A bilayer model of human atria: mathematical background, construction, and assessment

Simon Labarthe, Jason Bayer, Yves Coudière, Jacques Henry, Hubert Cochet, Pierre Jais, Edward Vigmond

A bilayer model of human atria: mathematical background, construction and assessment

Simon Labarthe, Jason Bayer, Yves Coudière, Jacques Henry, Hubert Cochet, Pierre~Jaïs and Edward Vigmond[1 2 3 4]

Abstract

(1) **Aims:** Atrial numerical modelling has generally represented the organ as either a surface or tissue with thickness. While surface models have significant computational advantages over tissue models, they cannot fully capture propagation patterns seen in vivo, such as dissociation of activity between endo- and epicardium. We introduce an intermediate representation, a bilayer model of the human atria, which is capable of recreating recorded activation patterns.

(2) **Methods:** We simultaneously solved two surface monodomain problems by formalizing an optimization method to set a coupling coefficient between them. Two different asymptotically equivalent numerical implementations of the model are presented. We then built a geometrically and electrophysiologically detailed model of the human atria based on CT data, including two layers of fibre directions, major muscle bundles, and discrete atrial coupling. We adjusted parameters to recreate clinically measured activation times. Activation was compared to a monolayer model.

(3) **Results:** Activation was fit to the physiological range measured over the entire atria. The crista terminalis and pectinate muscles were important for local right atrial activation, but did not significantly affect total activation time. Propagation in the bilayer model was similar

1 Simon Labarthe, Edward Vigmond, Jason Bayer, Yves Coudière and Jacques Henry are with the IMB, University Bordeaux I and University Bordeaux Segalen, 351 cours de la Liberation, 33405 Talence, France and Inria Bordeaux Sud-Ouest, 200 avenue de la Vieille Tour, 33 405 Talence, France.

2 Hubert Cochet and Pierre Jaïs are with the Hôpital Haut-Lévèque CHU Bordeaux, University Bordeaux Segalen, Avenue de Magellan, 33604 Pessac, France

3 All the authors are with the Electrophysiology and heart modeling institute LIRYC, PTIB – Campus Xavier Arnozan, Avenue du Haut Lévêque, 33600 Pessac, France.

4 Manuscript received ; revised .

to that of a monolayer, but with noticeable difference, due to three-dimensional propagation where fibre direction changed abruptly across the wall, resulting in a slight dissociation of activity.

(4) **Conclusion:** Atrial structure plays the dominant role in determining activation. A bilayer model is able to take into account transmural heterogeneities, while maintaining the low computational load associated with surface models.

Condensed abstract

An accurate bilayer model of human atria is introduced. Its mathematical fundations, realistic anatomical characteristics and electrophysiological implementation are described. A physiological activation pattern is assessed during sinus rhythm.

The bilayer model of atria demonstrates its capacity to model three-dimensional electrical activity while keeping a tractable computational load.

What's new

- A bilayer realistic model of human atria.
- The mathematical foundations, the geometry, anisotropy and electrophysiology implementation methodology are described.
- A physiological sinus rhythm activation pattern is assessed.
- Three dimensional electrical patterns are obtained with a weak computational load.

Introduction

Two modelling paradigms have been used to construct computer models of the electrical activity of the atria, surface modelling (1,2) and three-dimensional modelling (3–6). Surface models take advantage of the thinness of the atria to assume uniform transmural electrophysiological behavior and drastically reduce computation time as a consequence. A rigorous derivation of this type of model can be achieved by asymptotic analysis (7,8) using a very low ratio between the characteristic thickness of the tissue and the other dimensions. A strong limitation is that the asymptotic thickness for which those surface models give an accurate approximation of the 3D model is far below the physiological thicknesses observed. In addition, transmural properties are averaged, thus, the model is no longer suitable to analyze abrupt transmural variations. Conversely, when one considers that transmural heterogeneities are a major determinant of the complex mechanisms involved during electrical propagation in the atria, volumetric models are used with significant numerical cost.

We propose an intermediate model which is a bilayer representation of the atria, as first introduced by Gharaviri *et al.* (9). It is based on atrial physical structure (10), where distinct layers of aligned fibres can be discerned, with discrete coupling between layers. This approach is designed to reasonably capture three-dimensional behaviour at a computing load comparable to surface models. It is an enrichment of single surface representations because it

allows for transmural heterogeneities, and electrical dissociation (11).We have previously introduced a mathematical derivation of a bilayer model (8) wherein we proved convergence toward a 3D model for thin tissues. The simplicity of its mathematical expression has allowed us to analyze complex propagation inherent to the superposition of two distinct layers of tissue (8).

The construction of a reduced atrial model including both atria and transmural heterogeneities is a particularly useful tool to observe arrhythmic dynamics over long periods in a biatrial model (12). The goal of this paper is threefold:1) Formalization of the mathematical methods associated with the bilayer representation - section 1.1. This includes mathematical foundations of the bilayer approach with an equivalent formulation more amenable for implementation, and a methodology for optimizing the coupling coefficient for a given electrophysiological substrate; 2) Construct a detailed bilayer human atrial model - section 1.2; and 3) Assessment of how well the model captures 3D electrophysiological behavior - sections 1.3 and 2.

1 Methods

1.1 Bilayer mathematical model

We first introduce the mathematical expression of the bilayer model rigorously derived in a previous paper (8). We then focus on two versions of this approach. The first is the direct implementation which supplies a theoretical and numerical background and allows an evaluation of the approximation errors obtained, but employs nonstandard numerical techniques. The second one is an asymptotically equivalent formulation that can be directly implemented with existing finite element software able to mix elements of different dimensions.

1.1.1 Mathematical bilayer model

We want to solve on a surface domain ω and the layers $k=1,2$ the problem:

$$\begin{aligned}
&\beta(C_m\partial_t u_\gamma^{(k)} + I_{ion}^{(k)}(u_\gamma^{(k)},\zeta_\gamma^{(k)})) = \mathrm{div}_x(\sigma'^{(k)}\nabla_x u_\gamma^{(k)}) + (-1)^k\gamma(u_\gamma^{(1)} - u_\gamma^{(2)}) \\
&\partial_t\zeta_\gamma^{(k)} + g_{ion}^{(k)}(u_\gamma^{(k)},\zeta_\gamma^{(k)}) = 0
\end{aligned} \tag{1}$$

where β, C_m and γ refer respectively to the surface to volume ratio (1400 cm^{-1}), membrane capacitance (1 $\mu\mathrm{F}\,\mathrm{cm}^{-2}$) and the coupling coefficient between layers. The functions $\mathrm{I}_{ion}^{(k)}$, $\mathrm{g}_{ion}^{(k)}$ and $\sigma'^{(k)}$ describe respectively the transmembrane current density, transmembrane model, and the bidimensional conductivity tensor for each layer. The variables $\mathrm{u}_\gamma^{(k)}$ and $\zeta_\gamma^{(k)}$ are the transmembrane potential and the gating variables defined on layer k, both parameterized with γ. We remark that by two layers, we mean a unique geometric surface ω, but two different 2D diffusion tensors and ionic functions, allowing us to model transmural heterogeneities.

We showed in (8) that this model can be derived from the 3D problem on $\Omega = \Omega^{(1)} \cup \Omega^{(2)}$ where $\Omega^{(1)} = \omega\times]-h,0[$ and $\Omega^{(2)} = \omega\times]0,h[$:

$$\begin{aligned}
&\beta(C_m\partial_t u_{3d} + I_{ion}(u_{3d},\zeta_{3d})) = \mathrm{div}(\sigma\nabla u_{3d}) \\
&\partial_t\zeta_{3d} + g_{ion}(u_{3d},\zeta_{3d}) = 0
\end{aligned} \tag{2}$$

where for (X,z) $\in \Omega^{(k)}$, k=1,2

$$\sigma(X,z) = \begin{pmatrix} \sigma'^{(k)}(X) & & 0 \\ & & 0 \\ 0 & 0 & \sigma_3^{(k)} \end{pmatrix} \tag{3}$$

The coefficient $\sigma_3^{(k)}$ is then the transmural conductivity.

The asymptotic value of the coupling coefficient is $\gamma_a := \frac{3}{h^2}\frac{\sigma_3^{(1)}\sigma_3^{(2)}}{\sigma_3^{(1)}+\sigma_3^{(2)}}$. We see that γ gathers information on the thickness, h, and the transmural diffusion of the tissue. We also recall that γ is underestimated for physiological thicknesses (8), and that an optimal value has to be defined for a given set of tissue thickness, ionic model, and conductivity tensor. A convergence graph of the bilayer model can be seen in (13).

1.1.2 Alternative implementations of the bilayer model

1.1.2.1 Direct implementation

A semi-discrete finite-element version of Eqn. (1) can be written, for k=1,2:

$$M\beta(C_m\partial_t U^{(k)} + I_{ion}(U^{(k)}, \zeta^{(k)})) = -KU^{(k)} + (-1)^k \gamma M(U^{(1)} - U^{(2)}) \quad (4)$$

where the matrices M and K are the 2D mass and stiffness matrices on ω. The matrix γM collects the coupling coefficients between the layers. That coupling term imposes a specific implementation. We chose an alternative method, more suitable with the cardiac electrophysiology solver that we used : CARP (14).

1.1.2.2 Alternative implementation

To implement the bilayer model in an existing solver without additional code, we constructed two surfaces, ω_{endo} and ω_{epi}. Starting with ω_{epi}, ω_{endo} was produced by translating each point in the normal direction by a small distance ε. We then connected the points of the surfaces by linear elements L_i which are actually implemented as three-dimensional elements $L_i = S_i \times \varepsilon$, with base S_i and length ε. A P1 finite element semi-discrete formulation of this problem can be written:

$$\beta\left(M_k + \frac{\varepsilon}{3}S\right)\left(C_m\partial_t U^{(k)} + I_{ion}(U^{(k)}, \zeta^{(k)})\right) = -K_k U^{(k)} + (-1)^k \frac{\sigma_L}{\varepsilon} S\left(U^{(1)} - U^{(2)}\right) \quad (5)$$

where $k = 1$ corresponds to the endocardium, k=2 to the epicardium, and σ_L is the intracellular conductivity of the linear elements. S is a diagonal matrix whose i^{th} element is $|S_i|$ corresponding to the linear element that connects point i to its corresponding point in the other layer.

We see that when ε is small enough, the contribution of the linear element in the mass matrix can be neglected. Furthermore, by construction $M_1 \simeq M_2 \simeq M$ and $K_1 \simeq K_2 \simeq K$.

After these simplifications, the resulting system is asymptotically equivalent to the system (4) if $\frac{\sigma_L}{\varepsilon} S = \gamma M$.

The discretization of the two methods lead to asymptotically equivalent linear systems. In contrast, the second approach can be implemented without hard coding in a solver specialized in electrophysiological problems which is able to mix 1D and 2D elements.

1.1.3 Optimizing the coupling coefficient

We sought a γ that minimized the error on the activation maps of the bilayer solutions with respect to a 3D control model. We defined a 2D square ω and then solved the 3D problem (2) on $\Omega = \Omega^{(i)} \cup \Omega^{(2)}$ as defined previously . The 3D model had the same electrophysiology as the bilayer one, with fibres homogeneous throughout each layer but orthogonal between layers.

1.1.3.1 3D and 2D activation maps

We defined an activation map on layer $\Omega^{(k)}$ by averaging the potential over its thickness. The activation map $\mathrm{T}(\mathrm{u}_{3d}^{(k)})$ on layer k is then the function that maps the point $\mathrm{X} \in \omega$ to its first time of activation on the layer k :

$\mathrm{T}(\mathrm{u}_{3d}^{(k)})(X) = \min \left\{ t \in (0,T) \mid \frac{1}{|\Gamma^k|} \int_{\Gamma^k} u_{3d}(t,X,z).dz > \theta \right\}$, for the threshold $\theta = -60\mathrm{mV}$.

We get the activation map of the bilayer solution for a given γ on layer k as the function

$\mathrm{T}(\mathrm{u}_{\gamma}^{(k)})(X) = \min \left\{ t \in (0,T) | u_{\gamma}^{(k)}(t,X) > \theta \right\}$.

1.1.3.2 Optimization

To find γ, we minimized the relative $\mathrm{L}^2(\omega)$ norm of the difference in activation maps,

$$\min_{\gamma} \sum_{k=1,2} \frac{\|\mathcal{T}(u_{3d}^{(k)}) - \mathcal{T}(u_{\gamma}^{(k)})\|_{L^2(\omega)}}{\|\mathcal{T}(u_{3d}^{(k)})\|_{L^2(\omega)}} \tag{6}$$

by using Brent's method as implemented in the scipy library (15) that was interfaced with the cardiac electrophysiology solver CARP.

1.2 Geometrical Model construction

1.2.1 Imaging the atria

A biatrial geometry was clinically acquired from a healthy adult patient using ECG-gated contrast-enhanced multi-detector computed tomography (MDCT) with a voxel size of 0.5x0.4x0.4 mm. Precise characteristics of the acquisition can be found in a previous work (16). Transaxial images were imported in DICOM format into a local database of the software OsiriX 3.6.1 (OsiriX foundation, Geneva, Switzerland). The endocardial surface was segmented automatically using region growth segmentation. Volume rendering reconstructions were used to remove non atrial structures from the segmentation. Pulmonary veins were cut several centimeters from the ostia. The resulting segmentation was used to compute a 3D surface mesh in VTK format using CardioviZ3D (INRIA Asclepios, Sophia Antipolis, France) which further underwent weighted Laplacian smoothing. The acquired surface was treated as the epicardium.

1.2.2 General description of the model

We constructed the endocardial surfaces with $\varepsilon = 0.01\mathrm{cm}$. Note that this value does not represent the actual thickness, which is in the range 3--6.5 mm (17,18). In our model, thickness is taken into account with the definition of the optimal coupling coefficient - cf. subsection 1.1.3.

For the left atrium (LA), the endocardium was created by translating each point in the epicardium 100 μm in the inward normal direction, whereas in the right atrium (RA), the second layer modelled only the pectinate muscles (PM) and the crista terminalis (CT). Three

transeptal structures were manually added to the mesh to ensure LA - RA electrical connectivity : Bachmann's bundle (BB), the rim of the fossa ovalis (FO) and the coronary sinus (CS). An area of block was added between the sinus node (SAN) and the septum to isolate the SAN as observed by optical mapping (19) (Fig.1(a-d)). The final mesh contained 361,483 nodes and 715,034 triangular elements with an average diameter of 0.492 mm.

1.2.3 Fibre architecture

The fibre orientation was included with semi-automatic tools previously introduced (16). It reproduces histological descriptions (17,18) of the fibre architecture in the atria.

1.2.3.1 Right atrium

Histological studies have identified two regions in the RA, separated by the CT (17).

One region is directed towards the septum, characterized by a regular muscle structure, and the other region is located in the appendage, characterized by the presence of the PM covered by a more regular thin layer of myocytes. We defined one layer of our model to cover the entire RA. Its main fibre structures included a network of fibers from the septum which wrapped around the superior veina cava (SVC) and crossed the CT to cover the PM and insert into circumferential fibers of the vestibule. The endocardial layer only included the PM and CT with fibers oriented along these thick muscular structures -cf Fig.1(e-f).

1.2.3.2 Left atrium

Two layers comprised the LA, each of which covered the entire LA. On the anterior side, the epicardial fibers of the septo-pulmonary system are mainly circumferential and oblique, to reach the roof of the atrium and the mouth of the appendage. Conversely, the endocardial fibers of the septoatrial network are directed vertically to connect the vestibule to the dome of the LA. On the posterior side, transmural differences can be observed near the left inferior pulmonary vein(PV). If endocardial fibers are mainly oriented toward the septum, the epicardial fibers separate to blend into the vestibule to the septum and the appendage - cf.

Fig.1(g-h). The orientation of the fibers of the PV is usually more chaotic. We chose to simplify this fibre distribution and represent it by two layers with an orthogonal change in fibre direction. This choice corresponds to one of the numerous fibre orientation patterns observed in the PV (20), and can be easily revised if needed. The main differences in fibre orientation between layers are thus concentrated in the anterior wall of the PV and on the posterior part near the inferior left PV -cf. Fig.1(i).

1.2.4 Transeptal structures

The three transseptal structures correspond to the main transeptal connections identified in canines (21), and were taken into account in previous atrial models of normal conduction (3,22). Other smaller transseptal connections can be observed histologically (18), but with great inter-patient variability, and were discarded in this study. BB is identified as a rapid interatrial connection, the FO as a slower connection and the coronary sinus CS as masked during sinus activation.

1.2.4.1 BB

A manual segmentation of the 3D structure of the BB was made from the scanner image. In the RA, it wraps the SVC mouth by inserting into the fibre network of the anterior wall that connects the appendage to the FO. In the LA, it blends into the septo-pulmonary bundle of the epicardium that connects the FO to the left appendage and the PV. This three-dimensional structure was approximated by a two-dimensional structure: the mesh portions of the right and left atria are duplicated to model the insertion of the BB in the atrial tissue with a bilayer approach. Two bands provide the transseptal connections, an anterior and a posterior band. The anterior band was built by approaching a median surface of the initial three-dimensional structure. The posterior band was constructed from a rough discretization of a manually constructed surface, that we regularized and meshed with GMSH (23) and MeshLab (3D-COFORM Project , Italy) software - cf. Figure 1(b). The BB is connected with linear elements

to both endo and epi layers of the LA to model the blending of the BB fibres in LA musculature (17).

1.2.4.2 FO

The location of the FO was precisely identifiable from the segmentation of the atrium~: the two meshes intersected each other in this area. We removed the overlapping portions of the meshes and identified the boundaries of the holes thus created. We then built a two-dimensional strip joining the two boundaries with the same methodology previously used. See Fig. 1(c).

1.2.4.3 CS

The CS was not segmented in the initial mesh. A tubular structure was added to model its insertion into the posterior wall of the RA. A band connecting the CS to the RA vestibule was added with the previous procedure. See Fig. 1(d).

1.2.5 Model parameters and tissue heterogeneities

Cellular electrophysiology was described by the Courtemanche-Ramirez-Nattel model (24). Unique cellular electrophysiological properties were assigned spatially to the LA, RA, CT, BB, and PMs in the model as in (25). Further electrophysiological distinction was made for the appendages as in (4). See Table 1.

Tissue conductivities in the model were adjusted to produce activation times consistent with activation mapping data in patients -Table 3 in (26)- , and to preserve the conductivity ratios in (27). To keep conductivity values within the physiologic range for cardiac tissue ($\simeq 1\mathrm{S\,m^{-1}}$, cytoplasm), the maximal conductance for the sodium current (g_{Na}) was doubled uniformly over the entire atrial model. The maximal conductances and the tissue conductivity values determined for the bilayer model are presented in Table 1.

To determine γ, we performed the optimization described in § 1.1.3 with $\omega = 1 \times 1\mathrm{cm}$, $\mathrm{h}{=}0.2\mathrm{cm}$, for a total thickness of $0.4\ \mathrm{cm}$, and fibres orthogonal between layers. We used a

spatial discretization of $0.02\ \mathrm{cm}$. We differentiated γ in the RA and in the LA using appropriate electrophysiologic parameters as defined in Table 1. For the LA, both layers were atrial tissue, while in the RA, one layer was PM and the other was RA tissue. We obtained a value of $\sigma_L = 0.326\ \mathrm{S\,m^{-1}}$ for the coupling coefficient in the LA, and of $\sigma_L = 1.054\ \mathrm{S\,m^{-1}}$ for the RA. For the BB insertion, a $3\ \mathrm{S\,m^{-1}}$ conductivity was chosen to facilitate propagation through the BB-LA and BB-RA connections.

To observe activation patterns during sinus rhythm, after $10\ \mathrm{s}$ of quiescent activity in order to approach steady state, $2\ \mathrm{ms}$ long transmembrane current stimuli were applied to the SAN at twice diastolic threshold and a basic cycle length of $1000\ \mathrm{ms}$. All the simulations (sinus activation and compling coefficient fitting procedure) were ran with CARP using a fixed time step of 20 $\mu\mathrm{s}$ and a Crank-Nicolson scheme. On the PLAFRIM experimental testbed with Intel Xeon (R) X5550 2.66GHz processors, 4.5 seconds were approximatively required to simulate $1\ \mathrm{ms}$ of cardiac activity on 16 processors.

1.3 Methodology Assessment

1.3.1 Sinus wave characteristics

As described in section 1.2.5, tissue conductivities and sodium conductance were adjusted so that sinus activation reproduces qualitatively and quantitatively normal measured activation. To verify the regional parameters adjusted in the model, activation times in the model were averaged for each anatomical region in Fig.1(a) then plotted against the same regions with patient data (green vs. black traces Fig. 2(a)). To determine how essential the transmural and transeptal structures in the bilayer model were for matching the patient data, two additional simulations were ran. One with the endocardial layer detached from the epicardial layers, where propagation only occured in the epicardial layer without the influences of endocardial structures as the CT and PM in the RA (red trace Fig. 2(a)). This monolayer model will be designated from now on as the control model. The second without

the BB connections between the LA and RA to determine the role of transeptal structures in matching activation patterns observed in patients (blue trace Fig. 2(a)).

1.3.2 Three dimensional dynamics

We sought to ensure that our bilayer model captured three-dimensional phenomena of atrial electrical propagation.

1.3.2.1 Modification of conduction velocity

We first assessed how the addition of transmural heterogeneities of fiber direction modified sinus activation. In that goal, we compared the activation maps of the bilayer and control models. Noting u_b, the solution of the bilayer model, and u_c the solution of the control model, we calculated $\mathrm{T}(\mathrm{u}_b) - \mathcal{T}(u_c)$ on the epicardial layer, where T is defined in subsection 1.1.3.

1.3.2.2 Endo-epi electrical heterogeneities

The presence of electrical dissociation between the endocardial and epicardial layers was verified by computing the difference between the endo- and epicardial activation maps $\mathrm{T}(\mathrm{u}_b)_{|\Omega_{epi}} - \mathcal{T}(u_b)_{|\Omega_{endo}}$.

2 Results

2.1 Sinus activation and the role of transmural and transeptal structures

The bilayer model was able to produce an activation sequence well within the range of physiologically measured values, see Fig. 2. Specifically, the green trace in Fig.2(a) shows that the averaged local activation times at all regions in the bilayer atrial model were within reported patient data ranges (26). Fig. 2(e) shows the overall global activation in the model (118ms) was also within the patient data range (116$\pm$18ms).

Endocardial structures in the RA (CT,PM) were essential for matching early activation times, particularly in the right atrial appendage (RAA). As illustrated in Fig. 2(a) when comparing the red and black traces, without the CT and PM coupled to the myocardium, there

was a 32% increase in average activation time of the RAA. This slowing of propagation in the RA put activation times in the RAA out of the patient data range (69 ms vs. 39±21ms). Thus, the coupling of the CT and PM to the RA myocardium sets up a fast propagation pathway necessary to activate the RAA at times equivalent to those observed in patients.

Secondly, the importance of the BB transeptal structure for matching activation sequences in the LA of patients is illustrated by comparing the blue and black traces in Fig. 2(a). Without the BB transeptal structure bridging the RA to the LA, propagation from the RA to the LA has to go through the FO and CS. This abnormal propagation from the RA to LA significantly delays the activation time sequence of the pulmonary veins to outside the patient data ranges (Fig. 2(a)), in addition to, prolonging the overall global activation time by more than 36 ms to also be outside the global activation time measured in patients (154ms vs. 116±18ms).

2.2 Three dimensional dynamics

2.2.1 Bilayer and control models comparison

In Figures 3(a-b), we represent the activation time differences between the bilayer and the control models. We can observe that the differences are mainly located in the areas of high endo-epi differences of fibre directions. Thus, the RA appendage is activated faster in the bilayer model than in the control model by 30 ms. Similarly, slight differences were observed in the pulmonary veins and in the anterior wall of the LA vestibule, where the transmural fibre heterogeneity is maximal. The second layer then accelerates or slows the propagation, comparatively to the control model, depending on the relative orientation of the sinus wave and the fibres of the endocardial layer.

2.2.2 Electrical dissociation

2.2.2.1 Transmural electrical activation discrepancies

We can also observe differences in activation time between the endocardial and epicardial surfaces of the bilayer model - cf. Figures 3(c-d). These differences are still mainly located in

areas of transmural heterogeneities. We can see that in the PM, the epicardial layer is first activated - negative differences -, and when the endocardial layer is depolarized, the endocardial wave gathers with the epicardial wave in the mid-PM. On the tip of the PM, the endocardial wave passes the epicardial one. The endocardium is first activated - positive differences.

Differences can also be observed in the LA in the anterior and posterior faces and in the neighbourhood of the PV . The endocardial wave may be ahead - positive difference - or delayed - negative difference - compared to the epicardial wave , depending on the orientation of the fibres.

3 Discussion

In this paper we present a bilayer representation of the human atria. We extend the previous formulation of the bilayer approach (9), which was a planar model, by using a more complicated geometry based on patient data. We mathematically derive the parameters of the model, giving us a solid foundation for relating parameter values to physical properties. This was then demonstrated for a simplified system. Activation times over the entire atria were within clinically measured ranges. The model exploits atrial architecture to reduce dimensionality while retaining essential behavior. Computation cost is reduced dramatically. For example, given discretization of 250 μm, each millimeter of thickness would require 4 sheets, so that a 4 mm thick atrium would result in 8.5 times more nodes and an even greater factor increase in memory since the resulting finite element matrices would be 3D and have more entries per row. Thus, our model represents an order of magnitude reduction in computation time and memory. An additional advantage of the methodology is that, because of its simplicity, it did not require any modifications to our existing cardiac simulator.

3.1 Application

The choice to simulate two coupled layers is an *a priori* compromise between adding

three-dimensional heterogeneities and computational cost. Implementing a discrete change in coupling, as seems to be present across the atrial wall, is not straight forward in finite element models. More complex structures can be added locally to the bilayer model if needed: additional layers or three-dimensional elements can be integrated to realize a more heterogeneous electrophysiological substrate. Transmural heterogeneities of fibres direction or ionic models are naturally taken into account by varying σ_k and I_{ion} from one layer to another. While these quantities are known to intrinsically vary gradually across the ventricular wall, no similar gradient has been displayed in the atria, beyond gross endo- and epicardial differences (28,29). Indeed, if we consider that a 5 mm thick atrial wall is two distinct 2.5 mm layers, the argument for homogeneous properties within a layer becomes stronger.

While the computational savings using a bilayer model are obvious, advantages over monolayer models require elucidation. First, the adding of a second layer locally slows down the propagation of the activation wave, due to the different fibre orientation in each layer. Those local modification of conduction velocity is a critical feature during arrhythmia. Furthermore, the bilayer model can display dissociation of activity in the two layers. This may be important if scars are present but not fully transmural, leading to block only in one layer. Fibrotic tissue may also be inserted between the layers, leading to complete dissociation. Structures like the PM have been suggested as being part of reentrant circuits (30) and cannot be repreented in a single layer. Finally, electrograms are sensitive to local propagation. Therefore, a single wavefront will not give the same electrogram as two wavefronts travelling in different directions, especially in the RA.

3.2 Choice of coupling coefficient

A key step in the bilayer approach is the definition of the coupling coefficient. This coefficient summarizes the 3D dynamics, taking into account the transmural propagation and the thickness of the tissue, but also the relationship between the transmural diffusion and the

surface spread. If all quantities are known, an optimization process in a simplified 3D geometrical configuration can be used to obtain the equivalent coupling coefficient. However, measuring the coupling between the epicardial and endocardial layers experimentally in tissue is problematic. Biologically, we can try to estimate gap junction conductance and density along the interface surface, and convert these to discrete quantities. Given the difficulty of this, these values will probably have to be inferred based on interlayer propagation. If coupling is too low, activity will not propagate between layers and if too high, electrical dissociation is not possible. Thus, an intermediate value is sought which reproduces the observed behavior.

During sinus depolarization, this model displays slight 3D electrical effects such as dissociation and endo-epi propagation velocities differences, which are presented in Fig 3. However, more important endo-epi discrepancies can be expected during arrhythmic propagations, due to the complex three-dimensional activation and repolarisation patterns. This platform can be an interesting tool to investigate those kind of effects that were observed during atrial fibrillation (11). Putting the coupling coefficient to a null value results in a total electrical

insulation of the layers. This situation can model structural disconnection, such as the lack of

coupling between the PM and epicardium, for fibro-fatty tissue insertion between layers as may occur during remodelling due to disease (31).

3.3 Activation sequence

The activation sequence agrees very well with that measured physiologically (32). Notably, the first activation of the LA is located near the left superior pulmonary vein. One can also note that this model takes into account recent results concerning the emergence of the sinus wave at discrete points of atrial tissue (19) near the area of the SAN, which subtends the

hypothesis of a block line near the SAN. The total activation time, 118 ms, is in the range of physiological P-wave duration (32).

To fit this activation sequence, in addition to the optimized connection values, only the LA and RA tissue conductivities were adjusted to scale the activation sequences to within the clinically determined ranges. Thus, the major determinants of local activation are structural. In the RA, the propagation along the pectinate muscles and the crista terminalis were important for leading to an earlier activation of the RA appendage. This was an instance where interlayer coupling was important. The degree of coupling determined how much propagation along the PM accelerated propagation in the overlying layer, and, conversely, how much propagation in the PM was slowed due to loading. The PM are mostly disconnected from the RA free wall, especially over their central portion. This feature was not implemented in our model but can be easily added by locally setting the coupling parameter to zero. LA activation was primarily controlled by the insertion of BB. The complex LA fibre architecture leads to a more isotropic propagation. In reentrant situations, propagation along the coronary sinus and fossa ovalis may be more prominent. Once these geometrical features were implemented, many of which are known precisely from the imaging, sodium conductance and conductivities were set. Conductivity is better constrained than sodium channel current density, having a maximum value of 1 S/m, that of cytoplasm. It is probable that single cell models tend to underestimate sodium channel density since cell isolation, necessary for experiments upon which the models are built, destroys intercalated disks where most of the sodium channels are located and anchoring proteins (33). Thus, we adjusted sodium conductivity to get a proper global activation. We did not have to add any special regions of ionic heterogeneity beyond those already defined, i.e., the CT and Pms. The other regional ionic changes previously identified (Table 1) did not alter conduction velocity. Thus, we conclude that structure in the atria is primarily responsible for activation patterns

observed.

Local differences in the activation sequence between the control and the bilayer models can be observed in the LA, mainly in the anterior and posterior walls, where the endo-epi fibre orientation discrepancies are the highest (Figure 1(i)). Those zones also correspond to the main endo-epi activation times heterogeneities. (Figure 3). But the major differences are located in the RA appendage. We can therefore assume that the control model would not have the same properties of perpetuation of arrhythmias in the right atrium. The higher velocity for the bilayer model in this area increases the wavelength, and decreases the likelihood of functional block in the right appendage. In contrast, the control model could be more prone to the occurrence of blocks during episodes of arrhythmia.

3.4 Personalization

The model developed here can be considered as a generic model of atria. The description of the organization of fibres, of the transseptal connections and of the tissue heterogeneities were made on the basis of histologic publications describing generic features on the atria. Several lines of development to move towards greater personalization of the model can be identified.

We included in our model a septum that electrically insulates the left and right atria with three transseptal connections: the BB, the FO and the CS. Histological studies sometime find muscular bridges which also allow transeptal propagation but their number and location are highly patient dependent (18,21). Strategies to personalize these connections in order to optimize the sites of first activation to replicate P-wave as those discussed in (34) may be considered. To do this, automation of the construction of these connections needs to be improved, for example, by moving these structures to different sites using registration methods.

Fiber orientation in the model follows a rule-based method. Currently, these structures are

not measurable by *in situ* imaging techniques, so using rule-based methods of construction is usual (6,27,34).

3.5 Varying the thickness of the tissue

We consider two different characteristic thicknesses of tissue : the thickness corresponding to the areas where the two layers are coupled - LA, PM and CT - and that corresponding to areas where a single layer is modeled - RA. Variations in tissue thickness are not taken into account in a systematic way, but such changes can be easily implemented in our model. A map of coupling coefficients γ can be built and included in the bilayer model to simulate variations in thickness and some transmural heterogeneities. Indeed, the coupling coefficient is governed by two parameters: the thickness of the tissue h and the transmural conductivity of tissue. A decrease of the coupling coefficient can model an increase of the thickness of the tissue or a decrease of the transmural conductivity, e.g. in the presence of transmural fibrosis. However, this will not take into account effects of thickness within a layer, where a thin structure may be juxtaposed to a thick one.

In such cases, variation of the surface elements thickness can also be considered wherein all elements are considered as 3D with an additional factor defining the thickness (35). This is similar to the linear coupling elements where a cross-sectional area was required. To implement this approach, the local finite element matrices are simply multiplied by the thickness before global assembly. Using such a formulation, block can be observed when going from thin to thick elements and an increase in velocity when going in the other direction.

3.6 Limitations

Much of the atria can be sufficiently approximated by a bilayer description. However, some regions may exhibit complex fibre structure with orientation which may vary smoothly with depth and not abruptly. This fibre arrangement would be correctly captured by the

bilayer model : it suffices to take the mean of fibre direction in each layer. More complicated fibre structure such as blending layers, crossing layers or tongues of tissue are histologically observed, in particular near the pulmonary veins (36). In such cases, the model may fail to properly capture fine features of local propagation. However, this model is most suited to examine global behaviour over long periods of time, like examining arrhythmias, so these small discrepancies will not affect characteristics of the reentry.

4 Conclusion

This generalized bilayer model can be seen as an interesting modelling platform to investigate arrhythmia development over long periods. Full three-dimensional models are less adapted for such an application because of the significant computational load. This bilayer model can especially help to shed light on basic and clinical issues related to the impact of electrical disconnections or transmural heterogeneities between the endocardial and epicardial surfaces of the atria during arrhythmias.

Acknowledgment

This work was partially supported by an ANR grant as part of "Investissements d'Avenir" program reference ANR-10-IAHU-04 and by the ANR grant program reference ANR-13-MONU-0004-01. The research leading to these results has received funding from the European Union Seventh Framework Programme (FP7/2007-2013) under Grant Agreement HEALTH-F2-2010-261057. Funding to JDB was provided by the Whitaker International Program administered by the Institute of International Education. Simulations presented in this paper were carried out using the PLAFRIM experimental testbed, developed under the Inria PlaFRIM development action with support from LABRI and IMB and other entities: Conseil Régional d'Aquitaine, FeDER, Université de Bordeaux and CNRS.

Bibliography.

1. Jacquemet V, Virag N, Ihara Z, Dang L, Blanc O, Zozor S, et al. Study of Unipolar Electrogram Morphology in a Computer Model of Atrial Fibrillation. J Cardiovasc

Electrophysiol. 2003;14:S172–S179.

2. Al Abed A, Guo T, Lovell NH, Dokos S. Optimisation of ionic models to fit tissue action potentials: application to 3D atrial modelling. Comput Math Methods Med. 2013;2013:951234.

3. Harrild DM, Henriquez CS. A Computer Model of Normal Conduction in the Human Atria. Circ Res. 2000;87(7):e25–36.

4. Seemann G, Höper C, Sachse FB, Dössel O, Holden AV, Zhang H. Heterogeneous three-dimensional anatomical and electrophysiological model of human atria. Philos Trans R Soc Math Phys Eng Sci. 2006;364(1843):1465–81.

5. Muñoz MA, Kaur J, Vigmond EJ. Onset of atrial arrhythmias elicited by autonomic modulation of rabbit sinoatrial node activity: a modeling study. Am J Physiol Heart Circ Physiol. 2011 Nov;301(5):H1974–H1983.

6. McDowell KS, Vadakkumpadan F, Blake R, Blauer J, Plank G, MacLeod RS, et al. Methodology for patient-specific modeling of atrial fibrosis as a substrate for atrial fibrillation. J Electrocardiol. 2012;45(6):640 – 645.

7. Chapelle D, Collin A, Gerbeau J-F. A surface-based electrophysiology model relying on asymptotic analysis and motivated by cardiac atria modeling. Math Models Methods Appl Sci [Internet]. 2013; Available from: http://hal.inria.fr/hal-00723691

8. Coudiere Y, Henry J, Labarthe S. An asymptotic two-layers monodomain model of cardiac electrophysiology in the atria. submitted.

9. Gharaviri A, Verheule S, Eckstein J, Potse M, Kuijpers NHL, Schotten U. A computer model of endo-epicardial electrical dissociation and transmural conduction during atrial fibrillation. Europace. 2012;14(suppl 5):v10–v16.

10. Wang K, Ho SY, Gibson DG, Anderson RH. Architecture of atrial musculature in humans. Br Heart J. 1995;73:559–65.

11. Eckstein J, Maesen B, Linz D, Zeemering S, van Hunnik A, Verheule S, et al. Time course and mechanisms of endo-epicardial electrical dissociation during atrial fibrillation in the goat. Cardiovasc Res. 2011;89(4):816–24.

12. Labarthe S, Vigmond E, Coudière Y, Henry J, Cochet H, Jais P. Influence of Transmural Slow-Conduction Zones on the Long- Time Behaviour Of Atrial Arrhythmia. A Numerical Study with a Human Bilayer Atrial Model. CINC - Computing in Cardiology 2013 [Internet]. Zaragoza, Spain; 2013. p. 1187–90. Available from: http://hal.inria.fr/hal-00921262

13. Labarthe S, Vigmond E, Coudière Y, Henry J, Cochet H, Jais P. A Computational Bilayer Surface Model of Human Atria. FIMH 2013 - 7th International Conference on Fonctional Imaging and Modeling of the Heart [Internet]. London, United Kingdom: Springer; 2013. Available from: http://hal.inria.fr/hal-00802104

14. Vigmond EJ, Hughes M, Plank G, Leon LJ. Computational tools for modeling electrical activity in cardiac tissue. J Electrocardiol. 2003;36, Supplement 1(0):69 – 74.

15. Oliphant TE. Python for Scientific Computing. Comput Sci Eng. 2007;9(3):10–20.

16. Labarthe S, Coudière Y, Henry J, Cochet H. A Semi-Automatic Method To Construct Atrial Fibre Structures : a Tool for Atrial Simulations. CinC 2012 - Computing in Cardiology [Internet]. Krakow, Pologne; 2012. p. 881–4. Available from: http://hal.inria.fr/hal-00759191

17. Ho SY, Anderson RH, Sánchez-Quintana D. Atrial structure and fibres: morphologic bases of atrial conduction. Cardiovasc Res. 2002;54(2):325–36.

18. Ho S, Sanchez-Quintana D, Cabrera J, Anderson R. Anatomy of the left atrium: implications for radiofrequency ablation of atrial fibrillation. J Cardiovasc Electrophysiol. 1999;10(11):1525 – 1533.

19. Fedorov VV, Schuessler RB, Hemphill M, Ambrosi CM, Chang R, Voloshina AS, et al. Structural and Functional Evidence for Discrete Exit Pathways That Connect the Canine Sinoatrial Node and Atria. Circ Res. 2009;104(7):915–23.

20. Verheule S, Wilson EE, Arora R, Engle SK, Scott LR, Olgin JE. Tissue structure and connexin expression of canine pulmonary veins. Cardiovasc Res. 2002;55(4):727–38.

21. Sakamoto S-I, Nitta T, Ishii Y, Miyagi Y, Ohmori H, Shimizu K. Interatrial Electrical Connections: The Precise Location and Preferential Conduction. J Cardiovasc Electrophysiol. 2005;16(10):1077–86.

22. Vigmond EJ, Ruckdeschel R, Trayanova N. Reentry in a Morphologically Realistic Atrial Model. J Cardiovasc Electrophysiol. 2001;12(9):1046–54.

23. Geuzaine C, Remacle J-F. Gmsh: a three-dimensional finite element mesh generator with built-in pre- and post-processing facilities. Int J Numer Methods Eng. 2009;79(11):1309–31.

24. Courtemanche M, Ramirez RJ, Nattel S. Ionic mechanisms underlying human atrial action potential properties: insights from a mathematical model. Am J Physiol - Heart Circ Physiol. 1998;275(1):H301–H321.

25. Aslanidi OV, Colman MA, Stott J, Dobrzynski H, Boyett MR, Holden AV, et al. 3D virtual human atria: A computational platform for studying clinical atrial fibrillation. Prog Biophys Mol Biol. 2011 Oct;107(1):156–68.

26. Lemery R, Birnie D, Tang ASL, Green M, Gollob M, Hendry M, et al. Normal atrial activation and voltage during sinus rhythm in the human heart: an endocardial and epicardial mapping study in patients with a history of atrial fibrillation. J Cardiovasc Electrophysiol. 2007 Apr;18(4):402–8.

27. Krueger M, Schmidt V, Tobón C, Weber F, Lorenz C, Keller DJ, et al. Modeling Atrial Fiber Orientation in Patient-Specific Geometries: A Semi-automatic Rule-Based Approach. In: Metaxas D, Axel L, editors. Functional Imaging and Modeling of the Heart [Internet]. Springer Berlin Heidelberg; 2011. p. 223–32. Available from: http://dx.doi.org/10.1007/978-3-642-21028-0_28

28. Wang ZG, Fermini B, Nattel S. Repolarization differences between guinea pig atrial

endocardium and epicardium: evidence for a role of Ito. Am J Physiol. 1991 May;260(5 Pt 2):H1501–H1506.

29. Anyukhovsky EP, Rosenshtraukh LV. Electrophysiological responses of canine atrial endocardium and epicardium to acetylcholine and 4-aminopyridine. Cardiovasc Res. 1999 Aug;43(2):364–70.

30. Gray RA, Pertsov AM, Jalife J. Incomplete reentry and epicardial breakthrough patterns during atrial fibrillation in the sheep heart. Circulation. 1996 Nov;94(10):2649–61.

31. Eckstein J, Verheule S, de Groot NM, de Groot N, Allessie M, Schotten U. Mechanisms of perpetuation of atrial fibrillation in chronically dilated atria. Prog Biophys Mol Biol. 2008;97(2-3):435–51.

32. Markides V, Schilling RJ, Yen Ho S, Chow AWC, Davies DW, Peters NS. Characterization of Left Atrial Activation in the Intact Human Heart. Circulation. 2003;107(5):733–9.

33. Delmar M, McKenna WJ. The cardiac desmosome and arrhythmogenic cardiomyopathies: from gene to disease. Circ Res. 2010 Sep;107(6):700–14.

34. Krueger M, Schulze WW, Rhode K, Razavi R, Seemann G, Dössel O. Towards personalized clinical in-silico modeling of atrial anatomy and electrophysiology. Med Biol Eng Comput. 2012;1–10.

35. Vigmond E, Labarthe S, Cochet H, Coudière Y, Henry J, Jais P. A Bilayer Representation of the Human Atria. Conf Proc IEEE Eng Med Biol Soc [Internet]. 2013. p. 1530–3. Available from: http://hal.inria.fr/hal-00837671

36. Saito T, Waki K, Becker AE. Left atrial myocardial extension onto pulmonary veins in humans: anatomic observations relevant for atrial arrhythmias. J Cardiovasc Electrophysiol. 2000;11:888–94.

Figures

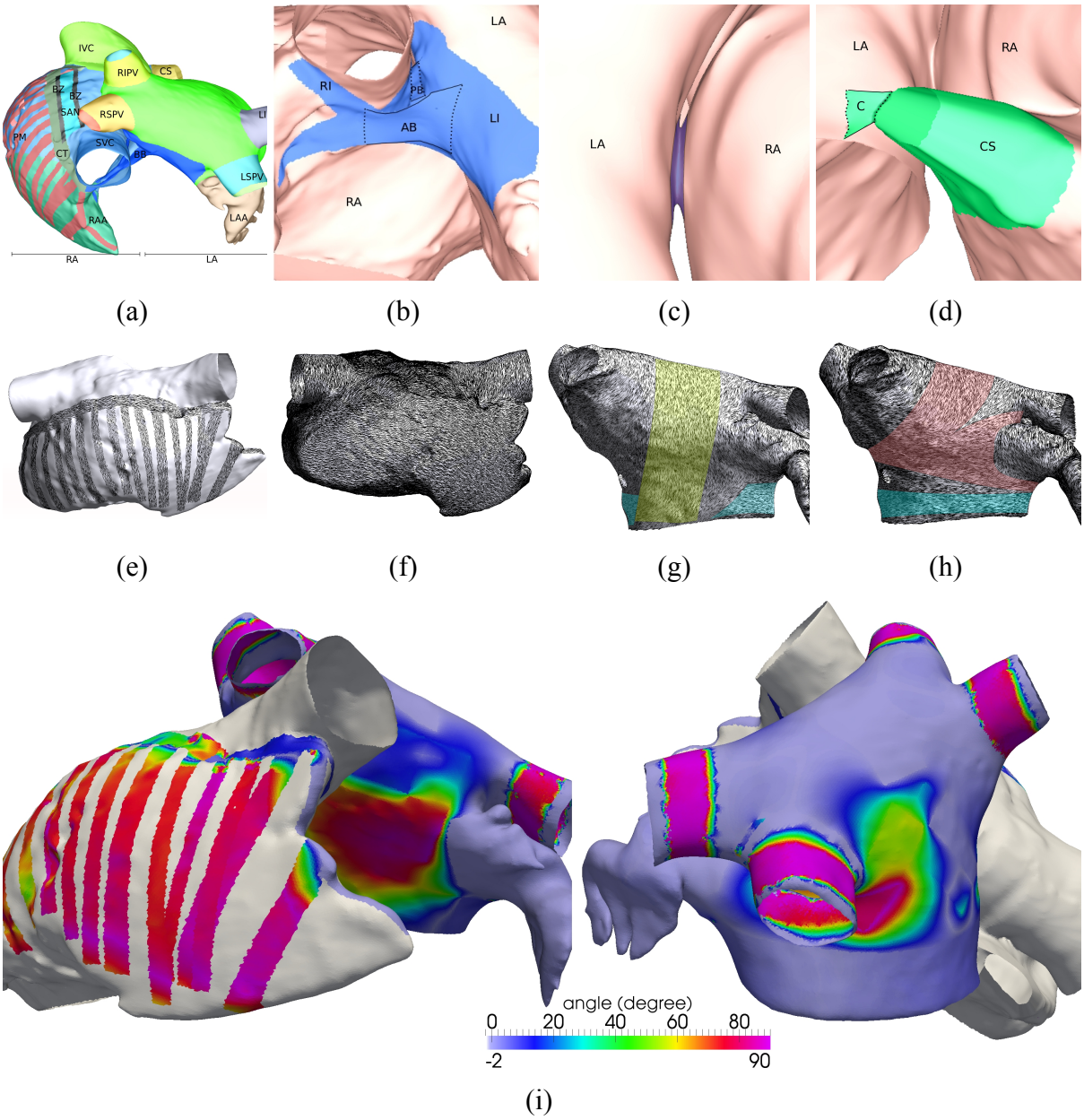

(a) (b) (c) (d)

(e) (f) (g) (h)

(i)

Figure 1: ***Geometrical characteristics of the bilayer model.***

First row. General view (a) and transseptal connections (b-d). *BB (blue), FO (purple) and CS (green) models are displayed. LA, RA: left and right atria. LI, RI : left and right insertions of the BB. AB, PB : anterior and posterior branches of the BB. C: connections between the CS and the LA.*

Second row. Fibre architecture. *Right superior view of the endo- (e) and epicardial (f) layers of the RA. Anterior view of the endo- (g) and epicardial (h) layers of the LA including the septoatrial (green) and septo-pulmonary (pink) bundles.*

Third row. Angle map: difference of endocardial and epicardial fibre direction, in degrees (i). *Gray (no value) : only one layer is defined. The main differencies are localised in the CT and the PM for the RA, and in the anterior and posterior walls and in PV for the LA.*

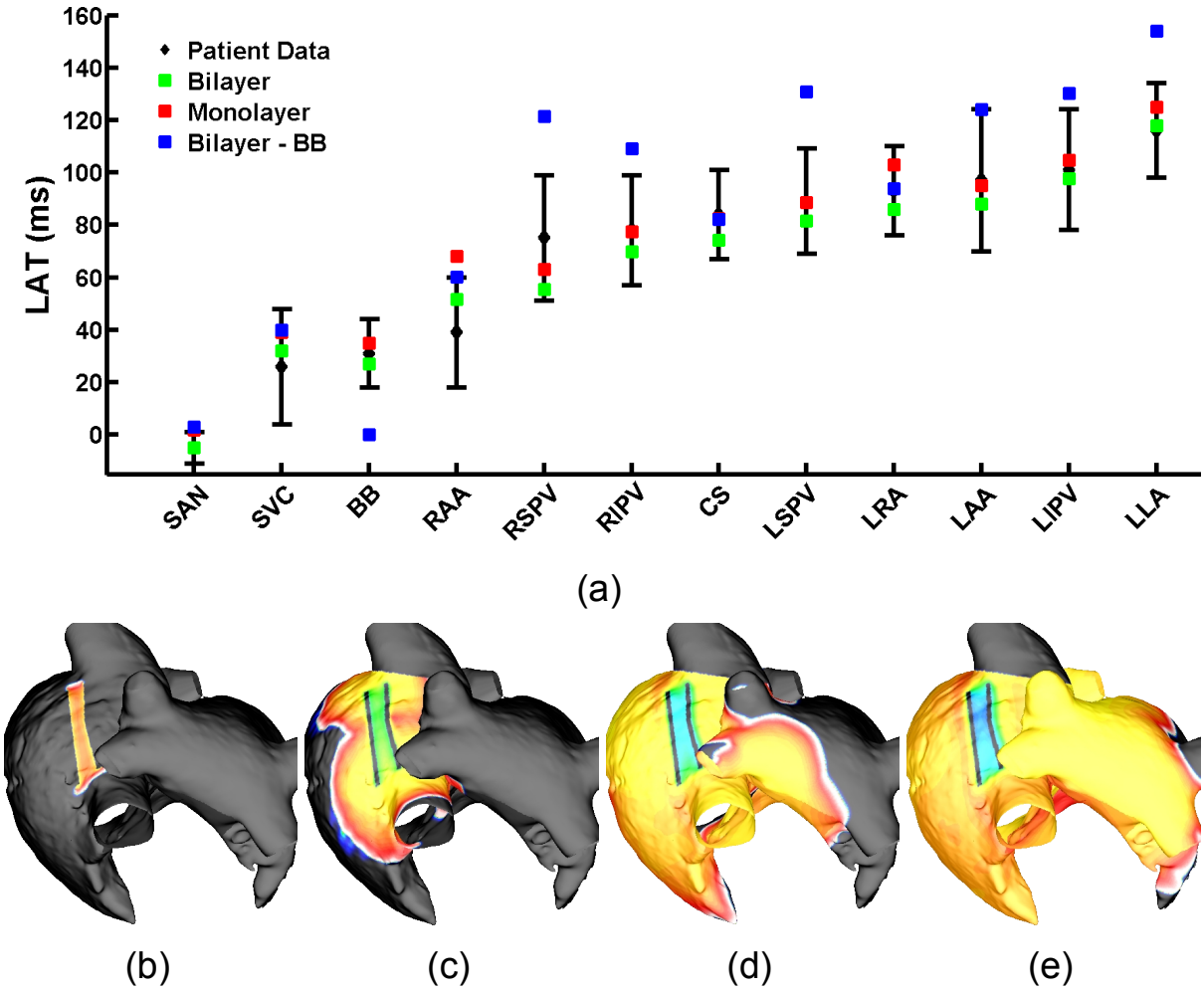

Figure 2: ***Activation properties.***

First row. Activation times: Patient vs. model (a). *Patient data in (26) is in black and the averaged activation times in the same anatomical regions of Fig. 1(a) for the bilayer simulation, epicardial monolayer (or control) simulation, and bilayer simulation without Bachmann's bundle connections. Sinoatrial node (SAN), superior vena cava (SVC), Bachmann's bundle (BB), right atrial appendage (RAA), right superior pulmonary vein (RSPV), right inferior pulmonary vein (RIPV), coronary sinus, (CS), left superior pulmonary vein (LSPV), latest right atrial activation time (LRA), left atrial appendage (LAA), left inferior pulmonary vein (LIPV), latest left atrial activation time (LLA).*

Second row. Activation sequence(superior anterior view). *(b): The SAN is depolarized. The sinus wave is rapidly gaining the CT and is distorted by its strong anisotropy. (c) The LA is depolarized by the posterior branch of the BB. In the RA, the PMs are activated and hasten propagation to the RAA. (d) The RA is closed to full activation. In the LA, the wave is distorted by the septo-pulmonary bundle and the BB insertion. (e) The entire atria is almost activated, ending by the LIPV, the tip of the LAA and the left posterior wall.*

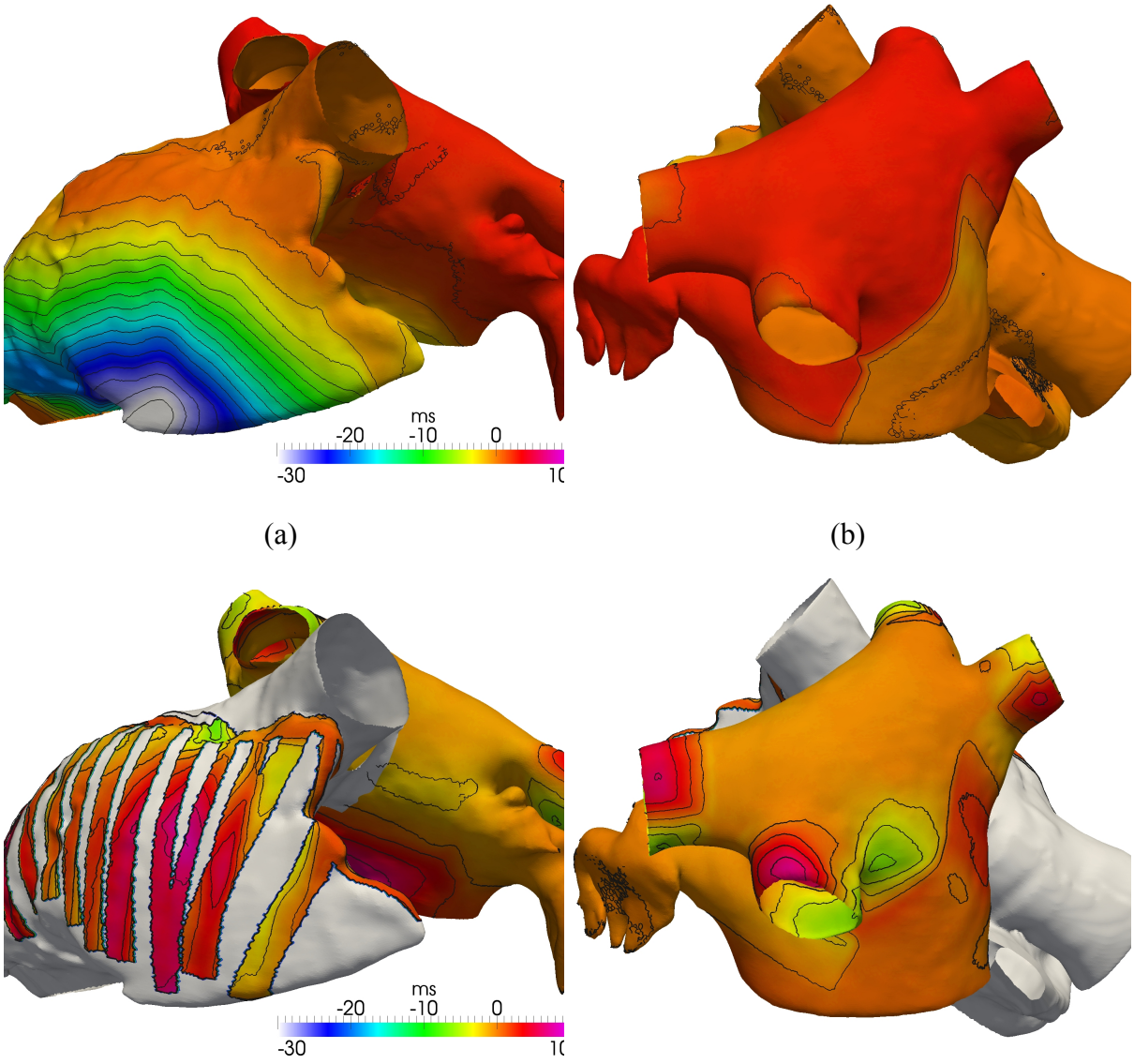

Figure 3: ***Three-dimensional activation properties.***

First row. Activation time differences between the bilayer and control models. *Right anterior (a) and left-posterior (b) views. The activation map of the control model was subtracted from the activation time of the bilayer model. Isochrones are displayed every 2 ms. We can observe a significant difference in activation time in the right appendage (30). The differences are slighter in the LA.*

Second row. Activation delays between the endo and epicardial faces. *Right anterior (c) and left-posterior (d) views. Isolines are displayed every 2 ms. Shaded areas represent areas without endocardial layer. The most important differences are mainly located in areas of transmural heterogeneity: the PM and PV. It should be noted that around the PV, the values are positive or negative, depending on the respective fibre orientation in both layer.*

Tables

	$\overline{g}_{Na}$	$\overline{g}_{To}$	$\overline{g}_{Kr}$	$\overline{g}_{Ca,L}$
RAA,LAA	2967.6	112.3	29.4	131.2
BB,CT	2967.6	211.5	29.4	206.7
PM	2967.6	165.0	29.4	123.8
LA	2967.6	165.0	47.0	129.4
RA	2967.6	165.0	29.4	129.4

Electrophysiological parameters

	g_l	g_t
SAN	0.392	0.392
BZ, IVC	0.001	0.001
CT	0.492	0.075
PM	0.695	0.03
BB	0.702	0.181
Othe (default)	0.4	0.107

Conductivities

Table 1: Electrophysiological and conductivity heterogeneities : maximal conductances of I_{Na}, I_{To}, I_{Kr} and $I_{Ca,L}$, and longitudinal (g_l) and transverse (g_t) conductivities for different zones.